Journal of Alloys and Compounds 936 (2023) 168138

Contents lists available at ScienceDirect

Journal of Alloys and Compounds

journal homepage: www.elsevier.com/locate/jalcom

Elucidating the optimized P2 type $Na_{0.67}Mn_{1-x}Cu_xO_2$ cathode active material via operando XAS

S. Altin [a], S. Altundag [a], E. Altin [b], D.E.P. Vanpoucke [c], S. Avci [d], M.N. Ates [e,*]

[a] Physics Department, Inonu University, 44280 Malatya, Turkey
[b] IBTAM, Inonu University, 44280 Malatya, Turkey
[c] UHasselt, Institute for Materials Research and IMEC vzw, IMOMEC, Agoralaan, 3590 Diepenbeek, Belgium
[d] Department of Physics Engineering, Istanbul Medeniyet University, Istanbul, Turkey
[e] TÜBİTAK Rail Transport Technologies Institute, Energy Storage Division, TÜBİTAK Gebze Campus, 41470 Gebze, Kocaeli, Turkey

ARTICLE INFO

Article history:
Received 19 August 2022
Received in revised form 13 November 2022
Accepted 17 November 2022
Available online 19 November 2022

Keywords:
Na0.67MnO2
Cu-substitution
Na-ion
Operando XAS

ABSTRACT

Here we report on the structural and electrochemical properties of P2-type $Na_{0.67}Mn_{1-x}Cu_xO_2$ (where x = 0.20–0.50) via various techniques. X-ray diffraction (XRD) reveals a reduction of the unit cell volume upon substitution of Cu elucidated through detailed Rietveld analysis. The cyclic voltammetry (CV) behavior is also affected by the Cu substitution indicating new redox reactions stemming from Cu substitution. Galvanostatic cycling measurements at room temperature show that when x = 0.35 in a P2-type $Na_{0.67}Mn_{1-x}Cu_xO_2$ cathode active material, the best electrochemical performance is obtained. The Na-ion diffusion rate is found to be strongly dependent upon the environmental temperature. Changes in the valence state and the local structures of P2-type $Na_{0.67}Mn_{1-x}Cu_xO_2$ during the charge/discharge are investigated through the operando X-ray absorption spectroscopy (XAS) technique.

© 2022 Elsevier B.V. All rights reserved.

1. Introduction

Manganese-based cathode active materials for both rechargeable Li and Na ion batteries have received great attention due to their low production cost, high specific energy, and low toxicity [1,2]. Na-ion batteries (NIBs) are becoming the `*holy grail*` of the next-generation battery technology as their active compounds are identical to that of li-ion battery counterparts. For NIBs, the most popular cathode active material is Na_xMnO_2 where the oxidation state of Mn changes between 3^+ and 4^+ during cycling [3] revealing a capacity of over 165 mAh/g [4]. The main disadvantage of Na_xMnO_2 is the Jahn-Teller distortion (JTd) due to the presence of Mn^{3+} ions [5]. When a Mn^{3+} ion with a high spin configuration ($t_{2g}^3e_g^1$) is placed in an octahedral environment, the energy of the system can go down due to the lowering of one of the e_g orbitals by elongation or compression of the bonds along the c-direction. In addition, insertion and removal of the Na-ions can trigger more changes along the c-axis causing significant geometric distortions adversely affecting the battery performance [6].

There are myriad studies in the literature for improving the battery performance of Na_xMnO_2 material by partial substitution of Mn by Ni, Li, Co, Al, Zn, Mg, and Cu [7–15]. Among these, Cu substitution is particularly intriguing as it increases the average potential during discharge and improves the specific capacity of the cathode material due to the redox active Cu^{2+}/Cu^{3+} couples [16]. Chen reported that $Na_{0.6}Mn_{0.9}Cu_{0.1}O_2$ reaches a capacity of 115 mAh/g (at 1 C rate) after 100 cycles with a capacity retention of 80% while the same material without Cu substitution reveals a capacity of 70 mAh/g after 100 cycles at the same rate with a capacity retention of 55% [17]. In addition, W. Kang et al. reported an increase in the average potential up to 3.37 V with Cu substitution, however, a decrease in capacity with increasing Cu content in $Na_{0.6}Mn_{1-x}Cu_xO_2$ (x = 0, 0.14, 0.25, and 0.33) [4]. The most studied composition of the Na-Mn-Cu-O cathode family is $Na_{0.67}Mn_{0.67}Cu_{0.33}O_2$ with a capacity value lower than 100 mAh/g at a relatively low rate [18]. Most of the studies reported so far in the literature utilize either sol-gel or co-precipitation methods for the synthesis of these Na-Mn-Cu-O compositions. However, these methods yield several impurity phases (such as CuO phases) along with the desired P2-$Na_{0.67}Mn_{0.67}Cu_{0.33}O_2$ phase [18–20]. Therefore, the Cu-substitution of Na_xMnO_2 should be investigated thoroughly to determine the optimum Cu content. It is well known that the substitution of the transition metals by another transition metal in the cathode

* Corresponding author.
E-mail address: mehmet.ates@tubitak.gov.tr (M.N. Ates).

https://doi.org/10.1016/j.jallcom.2022.168138
0925-8388/© 2022 Elsevier B.V. All rights reserved.

electrode materials for Li and Na-ion batteries are very common since they can still be redox active during charge and discharge of the batteries without distorting the lattice. One of the problems of the Na-ion battery cathodes is the inferior electrochemical performances, such as cycle life and rate capabilities, compared to Li-ion batteries. Cheng et. al. stated that the large energetic overlap between Cu 3d and O 2p states dictates the rigidity of oxygen framework, which effectively mitigates the structural distortion of local oxygen environment upon (de) sodiation and leads to the enhanced lattice reversibility for P2-$Na_{0.6}Mg_{0.15}Mn_{0.7}Cu_{0.15}O_2$ cathodes [21].

In this study, we report the detailed characterization, supported by the operando XAS of the P2-$Na_{0.67}Mn_{1-x}Cu_xO_2$ cathode material, where x is between 0.20 and 0.50. Structural and morphological characterization of the powders was performed by Fourier transform infrared spectroscopy (FTIR), scanning electron microscopy (SEM) coupled with Energy-dispersive X-ray spectroscopy (EDS), Raman Spectroscopy, X-ray Diffraction (XRD), Brunauer-Elmet-Teller (BET), and X-ray Absorption Spectroscopy (XAS) measurements. We also revealed the temperature dependence of the Na-ion diffusion rate via cyclic voltammetry measurements obtained at different temperatures. We found that Cu substitution causes the formation of additional redox reactions in the high voltage region. Furthermore, we performed operando XAS studies for the optimized $Na_{0.67}Mn_{0.65}Cu_{0.35}O_2$ cathode containing Na-ion cells and elucidated the changes in the valence states and local structures of the transition metal ions in the cathode active material.

2. Experimental section

Na_2O_2, CuO, and Mn_2O_3 were used in the stoichiometric amounts to synthesize $Na_{0.67}Mn_{1-x}Cu_xO_2$ where x varies between 0.20 and 0.50. The starting precursors were mixed in an agate mortar for 1–1.5 h and pressed into pellets under 5 tons. The pellets were further annealed at 900^0 C for 5 h in air and then quenched into liquid-N_2. The final samples were stored in a glove box where humidity and oxygen levels were kept below 5 ppm and 1 ppm, respectively.

XRD measurements were performed by a Rigaku RINT2000 diffractometer using CuK_α ($\lambda_{K\alpha}$=1.5405 Å) source. Structural details were determined via Rietveld refinement by using the GSAS-II software [22,23]. For Rietveld refinement, we used P63/mmc as reference cell symmetry which corresponds to P2-type structure. FTIR spectra of the samples were measured by a Perkin Elmer Spectrum One spectrophotometer. Surface morphology and EDS mapping analysis were obtained by a Leo EVO-40 VPX SEM combined with an EDS unit (Bruker X-flash detector 4010). Surface area of the powders was investigated by the Brunauer-Elmet-Teller (BET) technique using Micromeritics-TriStar 3000 at DAYTAM, Erzurum-Türkiye. Raman spectra of the samples were collected by NRS-4500 Confocal Raman Microscope using 532 nm laser at the AYBU-MERLAB, Ankara-Turkey. X-ray absorption near-edge (XANES) and extended x-ray absorption fine structure (EXAFS) analyses were performed at ROCK Beamline at SOLEIL in France. The XANES spectra and the EXAFS data at the Mn and Cu K-edges were collected in the transmission mode at room temperature. First, Mn and Cu foils were used for calibration and alignment purposes. This was followed by the real-time XAS measurements which were recorded during the cycling between a voltage window of 1.5–4.3 V at a C/10-rate. Details of the cell design in this study can be found in the literature [24]. Analysis of the XAS and EXAFS data were performed by Fastosh, Athena, and Artemis programs [25,26].

The cathode materials for the coin cells were fabricated by using $Na_{0.67}Mn_{1-x}Cu_xO_2$ powders. The active materials, Super-P carbon, and PVDF were mixed overnight in the NMP by the weight ratio of 70:15:15, respectively. The mixture was used for casting the slurry on Al foil with a 100 µm coating thickness by using a doctor blade. The films were held in a vacuum oven at 110 °C for 24 h for drying purposes. The electrodes were pressed by a rolling press, punched with a 15 mm diameter disc, and kept in an inert atmosphere. The active masses for each electrode were measured between 1.4 mg and 1.9 mg. The CR2032 cells were assembled according to half-cell configuration and Na foil was used as an anode material for 2-electrode configuration using 1 M $NaClO_4$ (PC/EC=50/50, w/w) as electrolyte.

The redox reactions were determined using the cyclic voltammetry (CV) technique between 1.5 V and 4.3 V with a scan rate of 0.1 mV s^{-1}. The CV measurements were performed with different scan rates at 5 °C, room temperature, and 50 °C to calculate the diffusion coefficients. The Ivium Octostat30 potentiostat/galvanostat integrated with NUVE EN-120 was used for the CV measurements under different environmental temperatures. Charge/discharge measurements up to 100 cycles were performed under constant current (CC-mode). C/3rate was chosen as the current density, and the measurements were conducted by Neware BTS4000 and Hefacycle BA100A battery analyzer at room conditions. Electrochemical Impedance Spectroscopy (EIS) studies were performed by ZIVE SP1 potentiostat/galvanostat from 0.1mHz to 200 kHz using 10 mV AC voltage.

3. Results and discussion

3.1. Structural properties

The $Na_{0.67}MnO_2$ crystallized in a hexagonal structure with $P6_3/mmc$ space group corresponding to the hexagonal $NaMnO_2$ structure in which 1/3 of the Na sites are empty. In this structure, the Mn and O ions are located at the Wyckoff positions of 2a and 24 l, respectively [27]. The Na ions are distributed over the two distinct Wyckoff positions namely 2b and 12j. Although the two Na positions have different Wyckoff notations, their local environment is identical. Substitutional studies for the $Na_{0.67}MnO_2$ compound usually focus on the Mn site since it is the only site occupied by a redox-active transition metal [28]. Fig. 1(a) shows the XRD patterns of the $Na_{0.67}Mn_{1-x}Cu_xO_2$ powder samples where x varies between 0.20 and 0.50. The patterns for the samples in which $x \leq 0.40$ match well with the hexagonal P2-type $Na_{0.67}MnO_2$ structure. The Rietveld analysis of the XRD pattern confirms the formation of the hexagonal crystal lattice with $P6_3/mmc$ space group (space group no. 193) [29]. The refined lattice parameters and Rwp values are given in Table 1. For the high Cu contents (especially $x > 0.4$), $Na_4Mn_9O_{18}$, Na_2O_2, Cu_2O, and CuO impurity phases begin to emerge. When x = 0.34, theoretically additional Cu ions need to be in a 3^+ valence state to compensate for the charge balance in the $Na_{0.67}Mn_{1-x}Cu_xO_2$ structure (cf., Fig. S1). Fig. 1(b) reflects the changes in the 2θ position of the (002) plane upon Cu substitution. From this figure, there is a clear trend that as the Cu content increases the shift towards a higher angle also is triggered. To elucidate this behavior, one must understand the charging mechanism within the structure. T-R. Chen et al. reported that increasing the Cu content, up to x = 0.15 in $Na_{0.6}Mn_{1-x}Cu_xO_2$, shifts the (002) reflection to lower angles due to the formation of Cu^{2+} ions. They found that increasing the Cu content further causes the peak to shift to higher degrees [20]. To interpret these results, it is crucial to understand how the Cu ions interact with the $Na_{0.67}MnO_2$ host lattice. In $Na_{0.67}MnO_2$, the Mn ions have two oxidation states to accommodate the charge equilibrium which are 1/3 Mn^{3+} and 2/3 Mn^{4+}. Substitution of Mn by Cu introduces Cu^{2+} ions and increases the Mn^{4+} ion fraction to satisfy the charge equilibrium. Such aliovalent substitution is a subject of interest due to the fact that an increase in Mn^{4+} fraction leads to decrease in Mn^{3+} ions with a high spin state. This further suppresses possible lattice distortions due to the Jahn-teller distortion effect [30]. In previous studies, to prevent these Jahn-teller distortions,

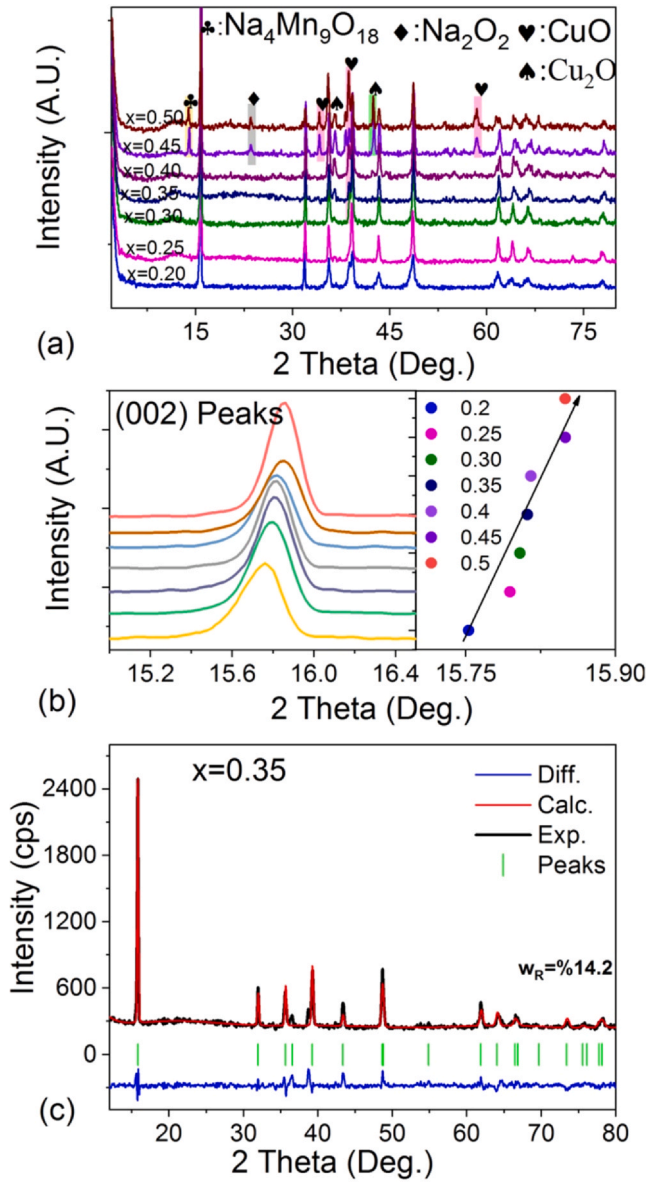


Fig. 1. (a) XRD patterns of $Na_{0.67}Mn_{1-x}Cu_xO_2$ samples (where x = 0.20–0.50), (b) (002) reflections of the samples (the right panel shows the maximum point of the (002) peaks) and (c) representative Rietveld refinement of the structure of x = 0.35 sample. $Na_4Mn_9O_{18}$ (PDF#27–0750), Na_2O_2 (PDF#15–0064), CuO (PDF#48–1548), and Cu_2O (PDF#34–1354) impurity phases were observed.

Mn^{3+} ions were substituted by Ni^{2+} and Mg^{2+} ions [29]. Similarly, Cu^{2+} ions have the potential to eliminate such distortions. Nevertheless, it should be mentioned that Cu^{2+} ions may also cause Jahn-Teller distortion depending on the environmental conditions. However, W. Kang et al. stated that the Cu substitution alleviates the strain between the c-axis and a-axis, which is helpful to suppress the Jahn–Teller effect of Mn^{3+} [4]. In addition, there is also a difference in radius between the various ions. As the Cu and Mn atoms are covalently bonded with O, Shannon crystal radii are the best suited values to define atomic radius [31]. These tabulated values are function of both oxidation state and atomic coordination and have been effectively used to predict the lattice expansion and contractions for the simple doped oxide systems [32,33]. Relevant Shannon values for Cu and Mn ions are presented in Table S1. Considering the crystal radii for the different oxidation states and coordination environments, it is interesting to note that 4-coordinated Cu^{2+} has almost the same crystal radius as 6-coordinated $Mn^{3+(LS)}$. In contrast, 6-coordinated Cu^{2+} is significantly larger than Mn^{3+}. This means that the coordination of Cu has crucial importance. In the $Na_{0.67}MnO_2$ structure, the Mn atoms are located in a 6-coordinated environment [34], allowing us to reasonably assume a 6-coordination environment for the substituted Cu atoms. However, if we consider general $NaCu_nO_{n+1}$ compounds, one can easily find planar CuO structures with 4-coordinated Cu (see Table S2) [35]. Furthermore, modelling work of Kim et al. on Na_xMnO_2, shows the crystalline structure to be rather complex, hosting three different coordination's for the five different Mn sites in $Na_{0.44}MnO_2$ [36] with presenting square-pyramidal coordination. Previously, it was shown that the effective radius of an aliovalent dopant may correspond to a lower coordination number than that of the expected coordination environment from the host lattice [37]. These two considerations are likely to indicate that the Cu^{2+} ions may take on a (planar) 4-coordinated geometry in the $Na_{0.67}Mn_{1-x}Cu_xO_2$ compounds. Assuming the overall geometry of the system is retained, as suggested by our XRD results along with the charge equilibrium requirement, it is plausible to calculate the average crystal radius of the transition metal (TM) centers (Cu and Mn) as a function of Cu concentration. The results for the two possible coordinations for Cu^{2+}(4- and 6-coordination) and two possible spin states for Mn^{3+} (LS and HS) are presented in Fig. S1. With the exception of the combination of LS Mn^{3+} with 6-coordinated Cu^{2+}, the remainder of the possible scenarios lead to a decrease in average TM radius as a function of the Cu concentration, which translates into a decrease in the lattice volume. As Cu substitutions increase, such a decrease in the lattice volume manifests itself as a shift to larger angles in the XRD pattern. These theoretical predictions are observed in our experiments supported by Fig. 1**(b)**. Rietveld refinement run at GSAS II [22,23] for the x = 0.35 sample is shown in Fig. 1**(c)**. The lattice parameters obtained from the Rietveld

Table 1
Lattice parameters of the samples.

Sample	a (Å)	c (Å)	v (Å^3)	Production method	note	
$Na_{0.67}Mn_{0.86}Cu_{0.14}O_2$	2.84	11.20	78.09	Sol-gel	–	[4]
$Na_{0.67}Mn_{0.75}Cu_{0.25}O_2$	2.84	11.19	78.07		CuO impurity	
$Na_{0.67}Mn_{0.67}Cu_{0.33}O_2$	2.85	11.19	78.74			
$Na_{0.67}Mn_{0.67}Cu_{0.33}O_2$	2.90	11.18	81.40	Sol-gel	CuO impurity	[28]
$Na_{0.67}Mn_{0.67}Cu_{0.33}O_2$	–	–	–	Coprecipitation + solid state	Impurity Not assigned	[36]
$Na_{0.60}Mn_{0.9}Cu_{0.10}O_2$	2.89	11.29		Coprecipitation + solid state	Impurity Not assigned	[17]
$Na_{0.67}Cu_{0.28}Mn_{0.72}O_2$	2.88	11.24		Sol-gel	No impurity phase	[38]
x = 0.20	2.91 (1)	11.23 (3)	82.15 (4)	Quenching/solid state synthesis	Rwp= 14.2	This study
x = 0.25	2.91 (1)	11.20 (5)	82.14 (1)		Rwp= 13.4	
x = 0.30	2.91(1)	11.19 (2)	81.91(2)		Rwp= 14.3	
x = 0.35	2.90 (1)	11.18 (2)	81.57 (2)		Rwp= 14.2	
x = 0.40	2.90 (1)	11.17 (1)	81.43 (2)		Rwp= 14.0	
x = 0.45	2.90 (1)	11.15 (2)	81.39 (2)		Rwp= 13.2	

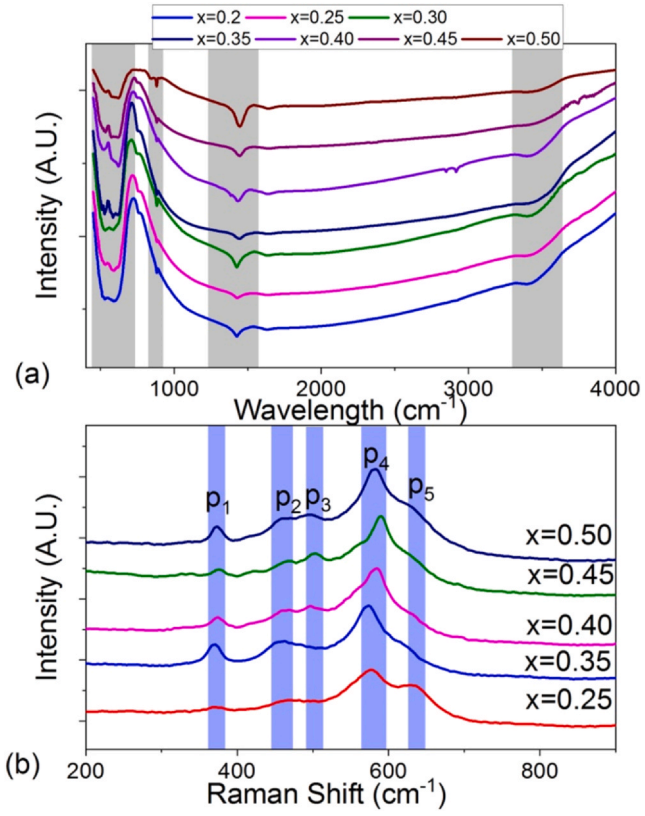


Fig. 2. (a) FTIR and (b) Raman spectra of $Na_{0.67}Mn_{1-x}Cu_xO_2$ samples (where x = 0.20–0.50).

refinements are listed in Table 1. Both a and c cell parameters and lattice volume have the highest value for x = 0.2 and decrease with increasing Cu content. According to phase analysis of the XRD patterns, the samples where x > 0.35 contain both Cu^+ (Cu_2O) and Cu^{2+} ions (CuO) and the Raman analysis supports the existence of both valence states which will be discussed later. Therefore, the peak shift to a higher angle in this study can be explained by the substitution of Mn by Cu. The resulting change of oxidation state from 3^+ to 4^+ of the remaining Mn atoms could also further reveal where Cu is doped.

FTIR spectra of P2-$Na_{0.67}Mn_{x-1}Cu_xO_2$ (x = 0.2–0.5) are shown in Fig. 2**(a)**. Bands at 505–674 cm^{-1} are due to Na-O [39] and Mn-O [40], respectively. The bands at 1430 cm^{-1} [41] and 3354 – 3607 cm^{-1} are related to Mn-O vibrations [42]. The changes in the intensities of the bands at 505–674 cm^{-1} and 3354 – 3607 cm^{-1} can be ascribed to the increasing Cu content. The FTIR bands of Cu-O are seen at 438, 517, and 590 cm^{-1}[43]. The broad peak noticed at 3433 cm^{-1} was attributed to O–H stretching of the moisture content [12].

The Raman spectra of the samples are shown in Fig. 2(b) where five different Raman active bands are visible. The corresponding structure for these bands is listed in Table S3**.** The bands denoted as P_2, P_4 and P_5 are related to manganese oxide vibration and stretching modes expected in all Na-Mn-O compounds [41–45]. Cu substitution causes the formation of new modes (P_1, P_3, and P_5) confirming the existence of Cu^+ (Cu_2O) and Cu^{2+} (CuO) ions. The amount of Cu^{2+} ions increase upon increasing the Cu content as can be traced by P_1 mode. The existence of Cu^+ can be clearly observed above x ≥ 0.40.

Elemental mapping of the samples where x = 0.20, 0.35, and 0.40, shown in Fig. S2 (a-c), confirms the homogenous dispersion of Cu and Mn in the samples. The results are consistent with the nominal contents of the elements and indicate an increase in the grain size as a function of increasing Cu content as seen in Table S4**.** The larger grains are expected to be structurally more stable than smaller grains due to their lower surface energy [20]. This is further supported by the surface area measurements of the respective samples by the BET method. The surface properties of the powders were analyzed by Brunauer-Emmett-Teller (BET) method as presented in Fig. S3. N_2 adsorption/desorption isotherm curves of powders have typical type II isotherm corresponding to microporous materials. The x = 0.35 compound has the largest specific surface area (34.16 m^2 g^{-1}) as listed in Table S5. The Barrett-Joyner-Halenda (BJH) pore size distribution curves of the samples are shown in the inset of Fig. S3. The surface area of the x = 0.35 sample showed the highest value among the others. Similar behavior can be seen in the literature where Mirasgari et. al. investigated the specific surface area change for the $LaCu_{0.5-x}Mn_xNi_{0.5}O_3$ (x = 0, 0.1, 0.3) and $LaCu_{0.4}Co_{0.1}Ni_{0.5}O_3$. They found that the highest surface area among the studied samples was for the sample of $LaCu_{0.2}Mn_{0.3}Ni_{0.5}O_3$. They further speculated that the substitution of Mn into the perovskite structure hindered the growth of crystallite that results in the higher meso-porosity. These changes in the crystalline size and the pore size distribution can lead to an improvement of the specific surface area [44]. We therefore postulated that the similar trend was observed in our case as well.

3.2. Electrochemical properties

Electrochemical properties of the cathode materials are strongly correlated with the local structure of the transition metal ions in rechargeable ion batteries. For instance, Chen et al. reported two redox reactions for $Na_{0.6}MnO_2$ in the CV curves; one is located at 2.2 V/2.4 V corresponding to the valence state change from Mn^{3+} to Mn^{4+}, and the second is placed at 3.4/3.6 V stemming from a biphasic transition observed in the tunnel structured Na-Mn based cathodes during Na insertion/removal. They didn't report any peaks above 3.6 V upon Cu substitution [46]. On the other hand, D. Sehrawat et al. delineate a redox reaction above 3.4 V in the Cu substituted Na_xMnO_2 materials reducing the electrochemical activity of Mn ions and improving the capacity retention [28]. W. Kang et al. attributed the peaks between 3.5 V and 4.1 V in the CV curves to Cu^{3+}/Cu^{2+} redox reactions in $Na_{0.67}Mn_{1-x}Cu_xO_2$ (x = 0–0.33) compositions were increasing the Cu content increases the potential value of the peaks [4].

W. Zuo et al. investigated the CV graphs of Na-Mn-O cathode materials and it was shown that the CV graphs can be divided into three regions: the anionic redox region (4 V <), the P2 phase region (2.5–4 V), and the Jahn Teller distortion region (> 2 V) [48 and 9–13–20–22–36]. The CV curves of the $Na_{0.67}Mn_{1-x}Cu_xO_2$ compositions are shown in Fig. 3. Two redox peaks can be noted for the compositions with low Cu content (x < 0.35) at 2.18 V/2.35 V (strong peaks) and 3.14 V/3.6 V (weak broad peaks), attributed to the local structural transitions of Na vacancies and Mn^{3+}/Mn^{4+} redox reactions [47], respectively. The compositions with 0.35 ≤x have two additional redox peaks at 3.91 V/4.01 V and at 3.56 V/3.7 V where the intensity of the peaks increases with increasing Cu content. We predicted that the redox reaction at 3.56 V/3.7 V is due to the biphasic transition of tunnel structure (due to Mn ions) as reported before which was observed for the low Cu content and the peaks around ~4.01 V related to Cu^{2+}/Cu^{3+} redox reactions [4,48–50].

The diffusion coefficient of Na-ions is an important parameter that directly affects the electrochemical performance and can be determined by the scan rate of the CV measurements. We performed CV measurements on the x = 0.35 sample with different scan rates at different temperatures i.e. 10 °C, room temperature, and 50 °C. Fig. 4 shows the CV curves run at a 0.6 mV/s scan rate at different temperatures. Fig. S4 further displays the CV curves with scan rates between 0.1 and 0.6 mV/s at different temperatures. In Fig. 4**,** the peak intensities and the voltage values of the cathodic peaks change as the temperature increases. The intensity of the oxidation peak above 4 V, corresponding to the Cu^{2+}/Cu^{3+} reaction, increases

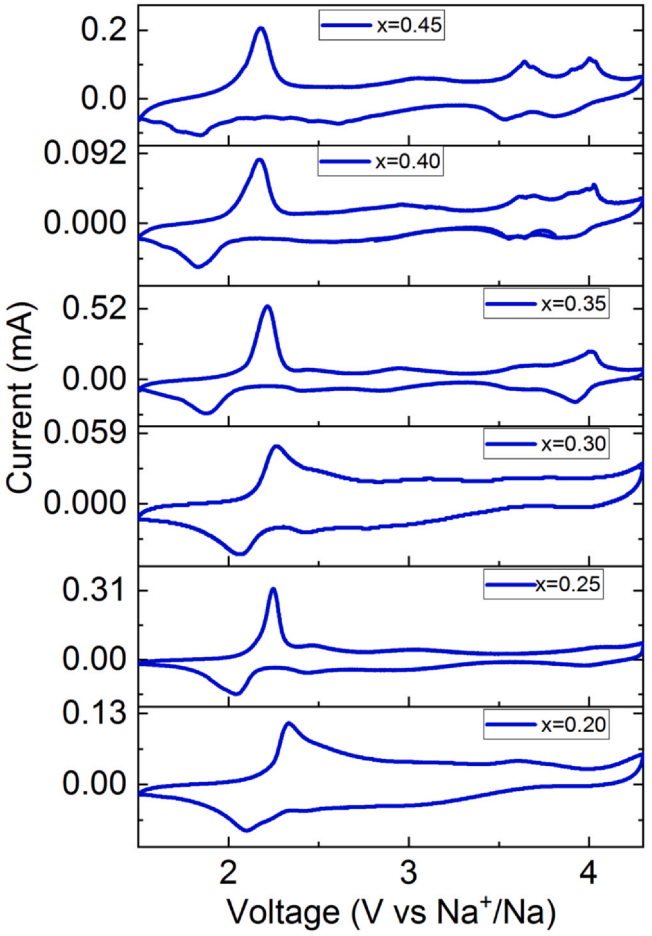


Fig. 3. CV graphs of $Na_{0.67}Mn_{1-x}Cu_xO_2$ where x varies between 0.20 and 0.50.

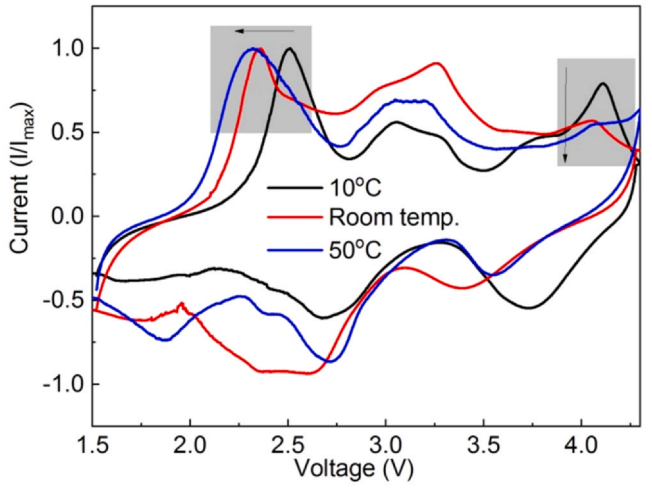


Fig. 4. CV graphs $Na_{0.67}Mn_{1-x}Cu_xO_2$ where x = 0.35 for 10 °C, room temperature using 0.6 mV/s scan rate and 50 °C. Y-axis is drawn I/I_{max} for comparison purposes.

significantly upon decreasing the temperature. In other words, low-temperature cycling affects the contribution of Cu ions during cycling. In our material, Mn and Cu ions share the same crystallographic sites but Mn^{3+} is expected to experience greater electrical attractive/repulsive force than that of Cu^{2+} ions due to their charges. In addition, thermal fluctuations during battery operations are expected to affect the insertion/removal kinetics of Na-ions [51]. Upon decreasing the working temperature, electrical attraction/repulsion effects may become more dominant than the other electrochemical contributions such as ion diffusion. This results in a more pronounced contribution of the Cu^{2+}/Cu^{3+} redox reaction than that of the Mn^{3+}/Mn^{4+} for Na-diffusion at low temperature i.e. 10 ^{0}C. A change in the voltage region of the Mn^{3+}/Mn^{4+} oxidation reaction is notable, i.e. 2.52 V, 2.36 V, and 2.31 V at 5 °C, room temperature, and 50 °C, respectively. The voltage value of a redox reaction is closely related to the energy that is used to remove Na-ions from their sites which is directly affected by the crystal field and the temperature. In our material, the shift in the voltage value of Mn^{3+}/Mn^{4+} oxidation reaction to lower voltage values upon increasing the temperature implies that Mn ions are oxidized more readily. As seen in Fig. 4, the redox reactions taking place between at 3–3.5 V attributed to the local structural transitions of Na vacancy and Mn^{3+}/Mn^{4+} orderings [47].

Temperature dependence of CV curves at 5 °C, room temperature, and 50 °C at different scan rates are shown in Fig. S4. There is a linear change between the CV peak current and the square root of the scan rate, where the diffusion coefficient of the Na-ions can be calculated by using the Randles–Sevcik equation provided below [52]:

$$I_p = 0.4463 \cdot n^{\frac{3}{2}} F^{\frac{3}{2}} \cdot C \cdot A \cdot R^{-\frac{1}{2}} T^{-1/2} D^{1/2} v^{1/2}$$

where the I_p is the peak current of CV, n is the number of electrons, F is the Faraday constant, C is the concentration of the Na-ions, A is the electrode surface area, R is the ideal gas constant, T is the Kelvin temperature, D is the diffusion coefficient, and v is the scan rate. The calculated D values for the x = 0.35 sample at 10 °C, room temperature, and 50 °C are listed in Table S6. The peak currents and voltages are clearly affected by the temperature. The I_p-$v^{0.5}$ $(V/s)^{0.5}$ curves of the x = 0.35 cells are shown in Fig. S5 and the slope of the I_p-$v^{0.5}$ curves were used to calculate the diffusion coefficients (Table S6).

Fig. S6(a-h) shows the voltage versus capacity curves for different cathode materials varying their Cu contents. The data are collected at a 10 mA/g current rate. The best battery performance is reached with the x = 0.35 sample with the highest initial and 100th cycle capacity value as seen in Fig. 5(a). Fig. 5(b) shows the capacity versus cycle number of all samples studied where the x = 0.35 sample has the lowest capacity fade over 100 cycles among other samples. Table S7 displays initial capacity denoted as C_1, and capacity after 100 cycles, denoted as C_{100}. Table S7 also compares the initial capacity values reported in various publications for similar material with different Cu contents. The x = 0.35 sample studied in this work has clearly superior electrochemical properties to the reported ones. It should be noted that the voltage window that we utilized is the widest range reported in the literature i.e. 1.5–4.3 V versus Na metal. During the discharge, a clear voltage plateau slightly above 2 V may be responsible for the higher capacity of the sample at x = 0.35. The differential capacity plot (dQ/dV) of the x = 0.35 cell is shown in Fig. 5(c) for the 1st, 50^{th,} and 100th cycles (Fig. S7 shows the dQ/dV plot for the other Cu compounds). The voltage values (as written in Fig. 5(c)) of the redox peaks for the Mn atom shift to higher values with increasing cycle numbers indicating possible lattice distortions and unwanted reactions in the cells. The redox peaks due to the Cu atoms can cause a decrease with the cycling of the cells and it is predicted that the deformation of the lattice is seen more Cu side than that of the Mn-site in the lattice.

Fig. 6 exhibits the cycling data at different rates for all the samples studied in this work. The different rates were performed with the current rates of 10 mA/g, 25 mA/g, 50 mA/g 100 mA/g, and 200 mA/g. It is further clear from this figure that the best rate performance was obtained for the compound where x = 0.35.

Fig. S8 shows EIS analysis results of $Na_{0.67}Mn_{1-x}Cu_xO_2$ where x = 0.20–0.45. The equivalent circuit model is presented in the inset. In the equivalent circuit, R_s and R_{ct} are the solution resistance and the charge transfer resistance between the electrode and electrolyte

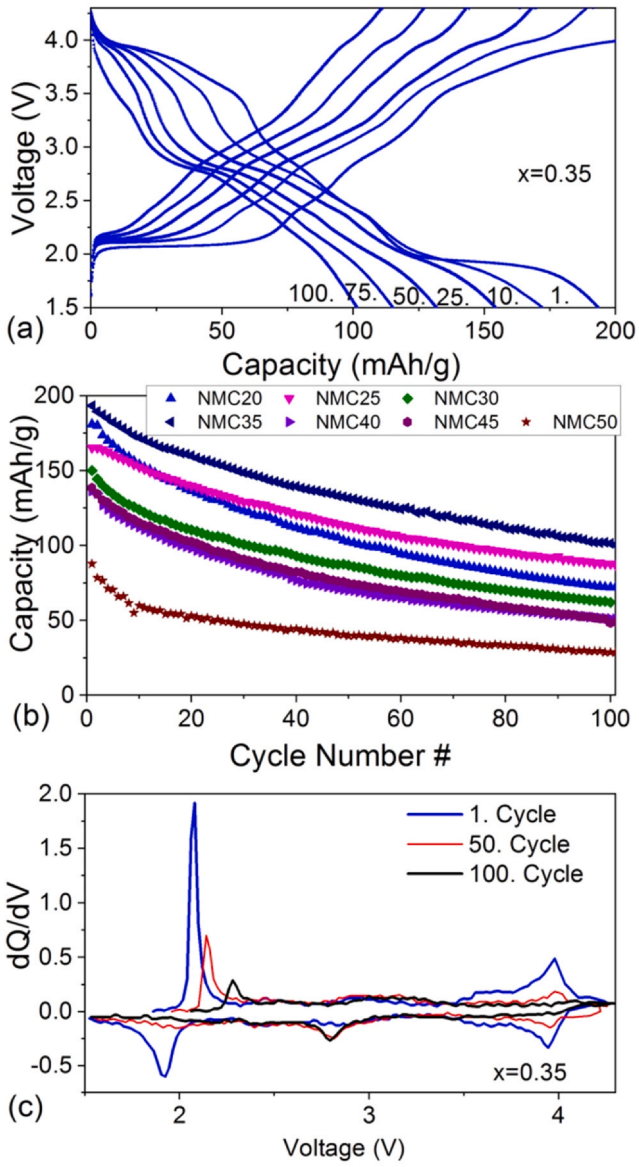


Fig. 5. (a) Voltage-Capacity measurement $Na_{0.67}Mn_{1-x}Cu_xO_2$where x = 0.35, capacity-cycle number graphs of $Na_{0.67}Mn_{1-x}Cu_xO_2$ where x = 0.20–0.50 and (c) dQ/dV-Voltage graphs of $Na_{0.67}Mn_{1-x}Cu_xO_2$ where x = 0.35.

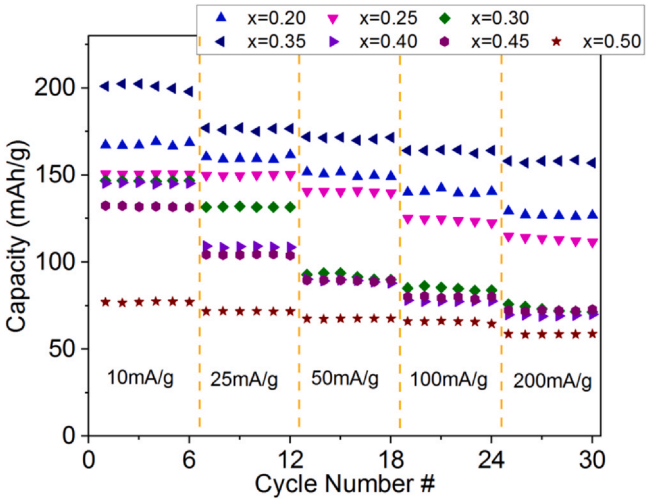


Fig. 6. Current density measurement of $Na_{0.67}Mn_{1-x}Cu_xO_2$ where x = 0.20–0.50.

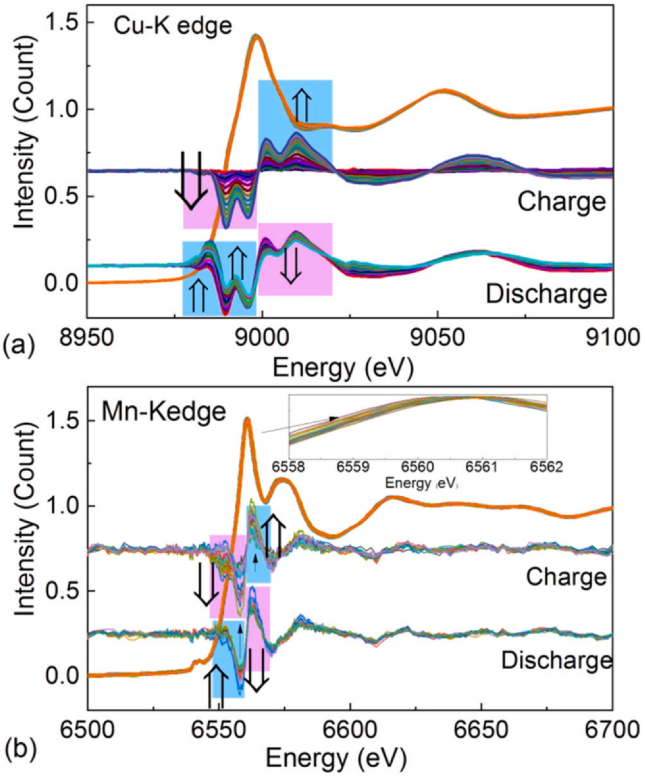


Fig. 7. (a) Cu and (b) Mn K-edge XANES of spectra of x = 0.35 during charge and discharge process. The curves indicated by the charge and discharge were calculated by subtracting of OCV XANES data. The blue boxes show the increase; the pink boxes indicate the decrease of the peak intensities.

interface, respectively. The semi-circle in EIS (R_{CT}) is due to Na^+ migration in the high-frequency region, and C_{int} is explained by the pseudo-capacitance at the interface between the electrode and electrolyte [53]. The Rs values can be found in the right panel of Fig. S8 showing the lowest value for x = 0.35. The radius of the semi-circle can give information about R_{ct} and similarly the lowest value is also observed for x = 0.35 indicating the lowest charge transfer impedance for this composition.

3.3. Operando XAS studies on the $Na_{0.67}Mn_{0.65}Cu_{0.35}O_2$ containing cell

In order to unravel the reaction mechanism centered at Cu and Mn atoms, we have further performed the operando XAS measurements for the valence state and the local structural changes. For this, we only studied the sample where x = 0.35 since it delivered the best electrochemical performances. Cu and Mn K-edge XANES spectra of the sample where x = 0.35 during charge and discharge processes are shown in Fig. 7 (a) and (b). During charging and discharging the clear change in the XANES spectra advocates valence state change. A shift in the XANES spectrum to higher energies is an indication of an increase in the valence state [54–62]. Such an increase in the valence state can be clearly seen in both Figures where during charging the energy shifted towards higher values. When the Na-ions leave their crystallographic sites during the galvanostatic charging process, the valence of the metal ions increases to higher values causing the XANES spectrum shifts to higher energies. The up and down signs indicated by arrows in XANES are pertaining to both Cu and Mn K-edges. An increase in the intensity of the curve differences between 8998 and 9020 eV upon charging is noticeable which indicates valence state change from Cu^{2+} to Cu^{3+} as expected. A similar phenomenon can also be seen for Mn^{3+} to Mn^{4+} albeit lesser resolution due to the fact that both Mn and Cu edges were run with the same

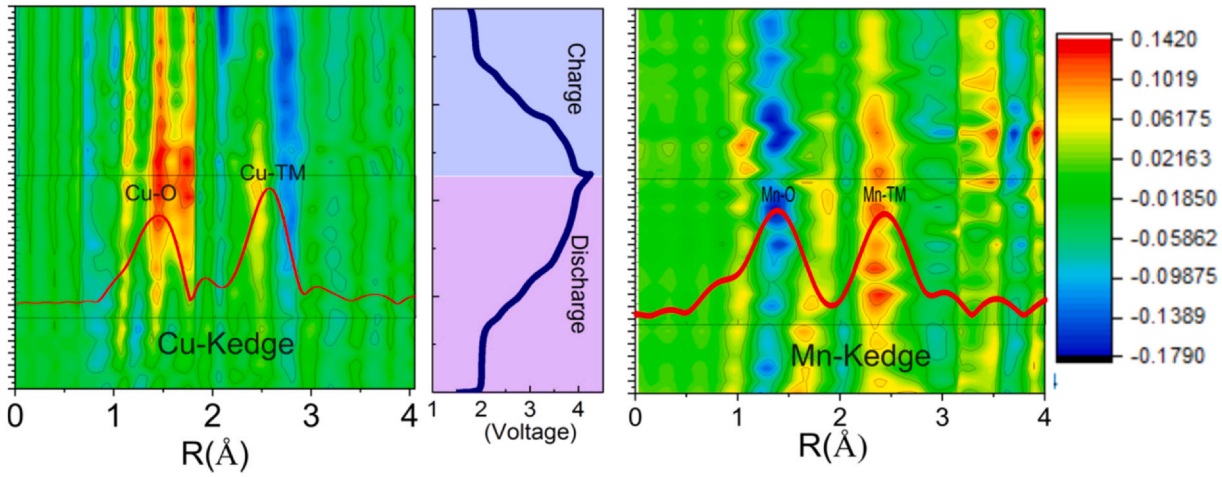


Fig. 8. The counterplot of FT of EXAFS for Cu and Mn K-edge during to charge and discharge process of $Na_{0.67}Mn_{1-x}Cu_xO_2$ where x = 0.35. The mapping data was calculated using OCV FT of XAS for Cu and Mn K-edge and it was subtracted from the FT of XAS graphs for different voltages.

gain value at the beamline. In order to obtain both Mn and Cu edges simultaneously, we had to increase the gain of the transmission mode which caused saturation to the Mn edge to some extent as the Mn concentration is much higher than Cu. Furthermore, the reverse trend can also be seen during discharge for both Mn and Cu atoms where the curve differences began to shrink back to the initial states.

To determine the local structure around Cu and Mn ions for the sample where x = 0.35, we performed Fourier Transform (FT) EXAFS analysis of XAS data. The contour plots of the FT analysis were further plotted for both Cu and Mn local structures. As baseline subtraction, we first calculated the FT of the targeted elements during the resting period to obtain reference data. Fig. 8 displays the FT of both Cu and Mn K edges during the charge and discharge of the Na-ion cell. The first and the second peaks in FT of Cu and Mn EXAFS data correspond to the metal-oxygen and metal-metal bonds, respectively [56]. In the left panel of Fig. 8, the concentrated red regions on Cu EXAFS correspond to the voltage value of ~4 V (in the middle panel) for both charging and discharging cases which supports the CV data (Fig. 6) where we claimed that Cu oxidation takes place. The color changes were normalized based on the bond intensity for M-O and M-M with respect to reference values taken during the rest period of the cell i.e. OCV. The negative value represents the decrease in the intensity while the positive value reflects the increase in the intensity of either M-O or M-M bonds. Removing the Na-ions at above 4 V changes the bond lengths which are tabulated in Table 2. A similar case is valid for Mn K-edge data as well. While the intensity of the FT of the Mn-O bond region decreases for both charging and discharging cases, the FT of the Mn-Cu bond increases consistent with the redox reactions of Mn ions as explained in the CV data. T. Gholam et al. stated that the increase in the intensity of the M-O distribution is related to change in the local environment of the metals [63].

Calculation of the bond lengths was performed using the Artemis program [64]. The representative fitting process at different states of the charge is shown in Fig. S9. The EXAFS equation is related to the scattering path of photoelectrons. The fitting parameters should be optimized for each case in detail as suggested by the literature [65]. $P6_3/mmc$ symmetry was used for the calculations and the Cu and Mn fittings were performed using the first scattering path of the data. Since it is not easy to distinguish Mn and Cu sites at the atomic scale, we used one metal ion occupation for one site during the fitting. The best-fit values of the structural parameters are listed in Table 2 The coordination number of the first (Ni-O) and second shells (Ni-M, M = Ni or Co) was found to be~6. These results agree well with the previous studies on the similar compounds [66]. According to Table 2, it should be noted that the bond length of R_{Cu-O} and R_{Mn-O} decreases by charging process up to 4.3 V, and then it increases during discharge. When the R_{TM-TM} was considered, R_{Cu-TM} was decreased by the charging process, while R_{Mn-TM} was increased by the charging process. It is evident that the de-insertion of Na-ions causes the increase in the freedom of the oxygen ions around Mn ions and they are attracted to Cu ions. In this case, there is more energy to the excitation of Cu ions for the contribution of redox reactions which support the CV analysis of the samples. Debye-Waller factor (σ^2) is related to the correlation of atomic motion in the structure and can give information on the vibrational dynamics of the structure, revealing displacements of atoms from their idealized positions [67]. So, σ^2 is expected to increase upon removal of Na-ions, and tabulated parameters in Table 2 support our argument.

Table 2
Artemis fitting parameters of x = 0.35 cells. (S_0^2 = 0.507 fixed, R range 1–3.4 Å and k = 3–16 $Å^{-1}$ for Cu and k = 3–10 $Å^{-1}$). The coordination number was fixed as 6 for the calculations.

Parameter	2 V	3.2 V	3.7 V	4.3 V	1.5 V
R_{Cu-O} (Å)	**1.952**	**1.942**	**1.942**	**1.942**	**1.955**
R_{Cu-TM} (Å)	**2.853**	**2.836**	**2.817**	**2.815**	**2.873**
σ^2_{Cu-O} x10^{-3}	**5.98**	**6.12**	**6.00**	**5.81**	**7.14**
σ^2_{Cu-TM} x10^{-3}	**6.28**	**6.20**	**6.00**	**5.75**	**3.88**
R-factor	**0.09**	**0.08**	**0.17**	**0.06**	**0.21**
RMn-O (Å)	1.907	1.900	1.897	1.897	1.894
RMn-TM (Å)	2.872	2.889	2.864	2.884	2.866
σMn-O x10–3	0.40	1.16	1.20	1.63	1.52
σMn-TM x10–3	1.88	2.98	2.44	2.91	2.58
R-factor	0.011	0.012	0.010	0.012	0.013

4. Conclusion

We successfully synthesized various Cu substituted $Na_{0.67}MnO_2$ samples via solid-state reaction technique followed by quenching. The XRD analysis shows that the samples have impurity phases of copper oxide when Cu substitution exceeds x = 0.35 in $Na_{0.67}Mn_{1-x}Cu_xO_2$. A decrease in the lattice volume as a function of increasing Cu content is attributed to the different ionic radii for the different coordination and valence states of the ions. FTIR and Raman measurements are consistent with the XRD results confirming the existence of multiple valence states of Cu ions. The highest surface area is found to be the x = 0.35 sample supported by the BET analysis. The redox peaks at the high voltage regions in the CV curves are attributed to the Cu ions which are more dominant at low temperatures than the Mn ions. We determined the optimum Cu

substitution as x = 0.35 due to its superior battery performance. The operando XANES analysis shows that the valence states of Cu and Mn are shifted to higher energies advocating simultaneous oxidations during charging. Operando EXAFS analysis demonstrated that majority of the Cu oxidation takes place close to the 4 V region while Mn oxidation follows a smooth and sluggish oxidation process covering almost entire charging potential. Refinement of EXAFS data were also performed to shed light on the atomic distance of TM-O and TM-TM.

CRediT authorship contribution statement

S. Altin: Methodology, Validation, Formal analysis, Investigation, Data curation, Writing, Visualization, Supervision, Project administration. **S. Altundag:** Validation, Formal analysis, Investigation, Resources. **E.A.:** Formal analysis, Investigation, Resources, Visualization. **D.E.P.V.:** Investigation, Formal analysis, Visualization, Data curation, Writing – review & editing. **S.Avci:** Validation, Formal analysis, Investigation. **I.I.G.:** Validation, Formal analysis, Investigation, Resources. **M.N.A:** Investigation, Formal analysis, Resources, Writing – review & editing, Supervision.

Data Availability

Data will be made available on request.

Declaration of Competing Interest

The authors declare that they have no known competing financial interests or personal relationships that could have appeared to influence the work reported in this paper.

Acknowledgment

The authors would like to thank Inonu University Research Council for project number FBA-2019-1960. The authors would like to thank Rock Beamline staff members in Soleil-France for the Operando XAS analysis and TENMAK for the financial support. M.N.A. greatly acknowledges the support from TÜBİTAK under the prestigious award of TÜBİTAK 2232 program.

Appendix A. Supporting information

Supplementary data associated with this article can be found in the online version at doi:10.1016/j.jallcom.2022.168138.

References

[1] I. Hasa, S. Mariyappan, D. Saurel, P. Adelhelm, A.T. Koposov, C. Masquelier, L. Croguennec, M. Casas-Cabanas, Challenges of today for Na-based batteries of the future: From materials to cell metrics, J. Power Sources 482 (2021) 228872, https://doi.org/10.1016/j.jpowsour.2020.228872

[2] J. Huanga, Z. Guo, X. Dong, D. Bin, Y. Wang, Y. Xia, Low-cost and high safe manganese-based aqueous battery for grid energy storage and conversion, Sci. Bull. 19 (2019) 1780–1787, https://doi.org/10.1016/j.scib.2019.09.020

[3] W. Zuo, Y. Yang, Synthesis, structure, electrochemical mechanisms, and atmospheric stability of Mn-based layered oxide cathodes for sodium ion batteries, Acc. Mater. Res. 3 (2022) 709–720, https://doi.org/10.1021/accountsmr.2c00058

[4] W. Kang, Z. Zhang, P.-K. Lee, T.-W. Ng, W. Li, Y. Tang, W. Zhang, C.S. Lee, D.Y. Wai Yu, Copper substituted P2-type $Na_{0.67}Cu_xMn_{1-x}O_2$: a stable high-power sodium-ion battery cathode, J. Mater. Chem. A 3 (2015) 22846, https://doi.org/10.1039/C5TA06371J

[5] Q. Liu, Z. Hu, M. Chen, C. Zou, H. Jin, S. Wang, S.-L. Chou, S.-X. Dou, Recent progress of layered transition metal oxide cathodes for sodium-ion batteries, Small 15 (2019) 1805381, https://doi.org/10.1002/smll.201805381

[6] R.J. Clement, P.G. Bruce, C.P. Greya, Manganese-based P2-type transition metal oxides as sodium-ion battery cathode materials, J. Electrochem. Soc. 162 (2015) A2589–A2604, https://doi.org/10.1149/2.0201514jes

[7] Y. Li, Z. Yang, S. Xu, L. Mu, L. Gu, Y.-S. Hu, H. Li, L. Chen, Air-stable copper-based $P2\text{-}Na_{7/9}Cu_{2/9}Fe_{1/9}Mn_{2/3}O_2$ as a new positive electrode material for sodium-ion batteries, Adv. Sci. 2 (2015) 1500031, https://doi.org/10.1002/advs.201500031

[8] C. Delmas, J.-J. Braconnier, C. Fouassier, P. Hagenmuller, Elecrochemical intercalation of sodium in Na_xCoO_2 bronzes, Solid State Ion. 4 (1981) 165–169, https://doi.org/10.1016/0167-2738(81)90076-X

[9] S. Komaba, W. Murat, T. Ishikawa, N. Yabuuchi, T. Ozeki, T. Nakayama, A. Ogata, K. Gotoh, K. Fujiwara, Electrochemical Na insertion and solid electrolyte interphase for hard-carbon electrodes and application to Na-ion batteries, Adv. Funct. Mater.. 21 (2011) 3859–3867, https://doi.org/10.1002/adfm.201100854

[10] A. Mendiboure, C. Delmas, P. Hagenmuller, Electrochemical intercalation and deintercalation of Na_xMnO_z bronzes, J. Solid State Chem. 57 (1985) 323–331, https://doi.org/10.1016/0022-4596(85)90194-X

[11] N. Yabuuchi, S. Komaba, Recent research progress on iron- and manganese-based positive electrode materials for rechargeable sodium batteries, Sci. Technol. Adv. Mater.. 15 (2014) 043501, https://doi.org/10.1088/1468-6996/15/4/043501

[12] S. Komaba, C. Takei, T. Nakayama, A. Ogata, N. Yabuuchi, Electrochemical intercalation activity of layered $NaCrO_2$ vs. $LiCrO_2$, Electrochem. Commun. 12 (2010) 355–358, https://doi.org/10.1016/j.elecom.2009.12.033

[13] N. Yabuuchi, H. Yoshida, S. Komaba, Crystal structures and electrode performance of alpha-$NaFeO_2$ for rechargeable sodium batteries, Electrochemistry 80 (10) (2012) 716–719, https://doi.org/10.5796/electrochemistry.80.716

[14] P. Vassilaras, X. Ma, X. Li, G. Ceder, Electrochemical properties of monoclinic $NaNiO_2$, J. Electrochem. Soc. 160 (2) (2013) A207–A211, https://doi.org/10.1149/2.023302jes

[15] K. Kubota, N. Yabuuchi, H. Yoshida, M. Dahbi, S. Komaba, Layered oxides as positive electrode materials for Na-ion batteries, MRS Bull. 39 (05) (2014) 416–422, https://doi.org/10.1557/mrs.2014.85

[16] L. Wang, Y.-G. Sun, L.-L. Hu, J.-Y. Piao, J. Guo, A. Manthiram, J. Ma, A.-M. Cao, Copper-substituted $Na_{0.67}Ni_{0.3-x}Cu_xMn_{0.7}O_2$ cathode materials for sodium-ion batteries with suppressed P2–O2 phase transition, J. Mater. Chem. A 5 (2017) 8752, https://doi.org/10.1039/C7TA00880E

[17] T.-R. Chen, T. Sheng, Z.-G. Wu, J.-T. Li, E.-H. Wang, C.-J. Wu, H.-T. Li, X.-D. Guo, B.-H. Zhong, L. Huang, S.-G. Sun, Cu^{2+} dual-doped layer-tunnel hybrid $Na_{0.6}Mn_{1-x}Cu_xO_2$ as a cathode of sodium-ion battery with enhanced structure stability, electrochemical property, and air stability, ACS Appl. Mater. Interfaces 10 (2018) 10147–10156, https://doi.org/10.1021/acsami.8b00614

[18] A. Gutierrez, W.M. Dose, O. Borkiewicz, F. Guo, M. Avdeev, S. Kim, T.T. Fister, Y. Ren, J. Bareño, C.S. Johnson, On Disrupting the Na^+-ion/vacancy ordering in P2-type Sodiummanganese-nickel oxide cathodes for Na^+-ion batteries, R1, J. Phys. Chem. 05537t (2018), https://doi.org/10.1021/acs.jpcc.8b05537

[19] V.H. Nguyen, M.L. Nguyen, H.P. Tran, V.M. Tran, N.T. Tran, M.L.P. Le, Cu-doped $NaCu_{0.05}Fe_{0.45}Co_{0.5}O_2$ as promising cathode material for Na-ion batteries: synthesis and characterization, J. Solid State Electrochem. 25 (2021) 767–775, https://doi.org/10.1007/s10008-020-04851-4

[20] L. Yang, S. Luo, Y. Wang, Y. Zhan, Q. Wang, Y. Zhang, X. Liu, W. Mu, F. Teng, Cu-doped layered P2-type $Na_{0.67}Ni_{0.33-x}Cu_xMn_{0.67}O_2$ cathode electrode material with enhanced electrochemical performance for sodium-ion batteries, Chem. Eng. J. 404 (2021) 126578, https://doi.org/10.1016/j.cej.2020.126578

[21] C. Cheng, C. Chen, S. Chu, H. Hu, T. Yan, X. Xia, X. Feng, J. Guo, D. Sun, J. Wu, S. Guo, L. Zhang, Enhancing the reversibility of lattice oxygen redox through modulated transition metal–oxygen covalency for layered battery electrodes, Adv. Mater. 34 (2022) 2201152, https://doi.org/10.1002/adma.202201152

[22] B.H. Toby, EXPGUI, a graphical user interface for GSAS, J. Appl. Cryst. 34 (2001) 210–213, https://doi.org/10.1107/S0021889801002242

[23] B.H. Toby, R.B. Von, Dreele, GSAS-II: the genesis of a modern open-source all purpose crystallography software package, J. Appl. Cryst. 46 (2013) 544–549, https://doi.org/10.1107/S0021889813003531

[24] Z. Wu, W.K. Pang, L. Chen, B. Johannessen, Z. Guo, In situ synchrotron X-ray absorption spectroscopy studies of anode materials for rechargeable batteries, Batter. Supercaps 4 (2021) 1547–1566, https://doi.org/10.1002/batt.202100006

[25] B. Ravela, M. Newville, Athena, artemis, hephaestus: data analysis for X-ray absorption spectroscopy using IFEFFIT, J. Synchrotron Rad. 12 (2005) 537–541, https://doi.org/10.1107/s0909049505012719

[26] G. Landrot, FASTOSH: a software to process XAFS data for geochemical & environmental applications, Goldschmidt Abstr. (2018).

[27] W. Zuo, J. Qiu, X. Liu, B. Zheng, Y. Zhao, J. Li, H. He, K. Zhou, Z. Xiao, Q. Li, G.F. Ortiz, Y. Yang, Highly-stable P2-$Na_{0.67}MnO_2$ electrode enabled by lattice tailoring and surface engineering, Energy Storage Mater. 26 (2020) 503–512, https://doi.org/10.1016/j.ensm.2019.11.024

[28] D. Sehrawat, J. Zhang, D.Y.W. Yu, N. Sharma, In situ studies of Li/Cu-doped layered P2 Na_xMnO_2 electrodes for sodium-ion batteries, Small Methods (2018) 1800092, https://doi.org/10.1002/smtd.201800092

[29] J.M. Paulsen, J.R. Dahn, Studies of the layered manganese bronzes, Na2/3[Mn1−xMx]O2 with M=Co, Ni, Li, and Li2/3[Mn1−xMx]O2 prepared by ion-exchange method, Solid State Ion.-. 126 (1999) 3–24, https://doi.org/10.1016/S0167-2738(99)00147-2

[30] K. Hemalatha, M. Jayakumar, P. Berac, A.S. Prakash, Improved electrochemical performance of $Na_{0.67}MnO_2$ through Ni and Mg substitution, J. Mater. Chem. A 3 (2015) 20908, https://doi.org/10.1039/C5TA06361B

[31] R.D. Shannon, Revised effective ionic radii and systematic studies of interatomie distances in halides and chaleogenides, Acta Cryst. A32 (1976) 751, https://doi.org/10.1107/S0567739476001551

[32] D.E.P. Vanpoucke, S. Cottenier, V.V. Speybroeck, P. Bultinck, I.V. Driessche, Tuning of CeO_2 buffer layers for coated superconductors through doping, Appl. Surf. Sci. 260 (2012) 32–35, https://doi.org/10.1016/j.apsusc.2012.01.032

[33] D.E.P. Vanpoucke, P. Bultinck, S. Cottenier, V.V. Speybroeckb, I.V. Driessche, Aliovalent doping of CeO_2: DFT study of oxidation state and vacancy effects, J. Mater. Chem. A 2 (2014) 13723, https://doi.org/10.1039/C4TA02449D

[34] Y. Zhang, S. Kim, G. Feng, Y. Wang, L. Liu, G. Ceder, X. Li, The interaction between Cu and Fe in P2-type Na_xTMO_2 cathodes for advanced battery performance, J. Electrochem. Soc. 165 (2018) A1184–A1192, https://doi.org/10.1149/2.0171807jes

[35] A. Jain, S.P. Ong, G. Hautier, W. Chen, W.D. Richards, S. Dacek, S. Cholia, D. Gunter, D. Skinner, G. Ceder, K.A. Persson, Commentary: the materials project: a materials genome approach to accelerating materials innovation, APL Mater. 1 (2013) 011002, https://doi.org/10.1063/1.4812323

[36] C.W. Mason, F. Lange, K. Saravanan, F. Lin, D. Nordlund, Beyond divalent copper: a redox couple for sodium ion battery cathode materials, ECS Electrochem. Lett. 4 (5) (2015) A41–A44, https://doi.org/10.1149/2.0041505eel

[37] H. Kim, D. Jun Kim, D.-H. Seo, M.S. Yeom, K. Kang, D.K. Kim, Y. Jung, Ab initio study of the sodium intercalation and intermediate phases in Na0.44MnO2 for sodium-ion battery, Chem. Mater. 24 (2012) 1205–1211, https://doi.org/10.1021/cm300065y

[38] W. Zheng, Q. Liu, Z. Wang, Z. Wu, S. Gu, L. Cao, K. Zhang, J. Fransaer, Z. Lu, Oxygen redox activity with small voltage hysteresis in $Na_{0.67}Cu_{0.28}Mn_{0.72}O_2$ for sodium-ion batteries, Energy Storage Mater. 28 (2020) 300–306, https://doi.org/10.1016/j.ensm.2020.03.016

[39] B. Nigam, S. Mittal, A. Prakash, S. Satsangi, P.K. Mahto, B.P. Swain, Synthesis and characterization of Fe_3O_4 nanoparticles for nanofluid applications-a review, Mater. Sci. Eng. 377 (2018) 012187, https://doi.org/10.1088/1757-899X/377/1/012187

[40] C.M. Julien, M. Massot, Vibrational Spectroscopy of Electrode Materials for Rechargeable Lithium Batteries III. Oxide Frameworks, Proceedings of the International Workshop, Advanced Techniques for Energy Sources Investigation and Testing, (2004) Sofia, Bulgaria.

[41] L. Ren, H. Qiu, W. Qin, M. Zhang, Y. Li, P. Wei, Inhibition mechanism of Ca^{2+}, Mg^{2+} and Fe^{3+} in finecassiterite flotation usingoctanohydroxamic acid, R. Soc. Open Sci. 5 (2018) 180158, https://doi.org/10.1098/rsos.180158

[42] A. Yuan, X. Wang, Y. Wang, J. Hu, Textural and capacitive characteristics of MnO_2 nanocrystals derivedfrom a novel solid-reaction route, Electrochim. Acta 54 (2009) 1021–1026, https://doi.org/10.1016/j.electacta.2008.08.057

[43] M. Elango, M. Deepa, R. Subramanian, A.M. Musthafa, Synthesis, characterization, and antibacterial activity of polyindole/Ag–Cuo nanocomposites by reflux condensation method, Polym. -Plast. Technol. Eng. 57 (14) (2017) 1440–1451, https://doi.org/10.1080/03602559.2017.1410832

[44] L. Debbichi, M.C. Marco de Lucas, J.K. Pierson, P. Krüger, Vibrational properties of CuO and Cu_4O_3 from first-principles calculations, and Raman and infrared spectroscopy, J. Phys. Chem. C 116 (2012) 10232–10237, https://doi.org/10.1021/jp303096m

[45] M. Mirasgari, S.M. Alavi, M. Rezaei, Effects of partial substitution of Cu by Mn and Co in LaCu0.5Ni0.5O3 catalyst synthesized by mechanochemical method in the total oxidation of methane, Res. Chem. Int. 48 (2022) 3811–3834, https://doi.org/10.1007/s11164-022-04775-w

[46] E. Kroumova, M.I. Aroyo, J.M. Perez-Mato, A. Kirov, C. Capillas, S. Ivantchev, H. Wondratschek, Bilbao crystallographic server: useful databases and tools for phase-transition studies, Phase Transit. 76 (2003) 155–170, https://doi.org/10.1080/0141159031000076110

[47] L.-C. Chen, C.-C. Chen, K.C. Liang, S.H. Chang, Z.-L. Tseng, S.-C. Yeh, C.-T. Chen, W.-T. Wu, C.-G. Wu, Nano-structured CuO-Cu_2O complex thin film for application in $CH_3NH_3PbI_3$ perovskite solar cells, Nanoscale Res. Lett. 11 (2016) 402, https://doi.org/10.1186/s11671-016-1621-4

[48] C.M. Julien, M. Massot, Lattice vibrations of materials for lithium rechargeable batteries III. Lithium manganese oxides, Mater. Sci. Eng. B 100 (2003) 217–230, https://doi.org/10.1016/S0921-5107(02)00582-2

[49] T.-J. Kima, D. Son, J. Cho, B. Park, Enhancement of the electrochemical properties of o-$LiMnO_2$ cathodes at elevated temperature by lithium and fluorine additions, J. Power Sources 154 (2006) 268–272, https://doi.org/10.1016/j.jpowsour.2005.03.193

[50] X. Fan, S. Zhang, Y. Zhu, J. Chen, Macroporous polymers prepared via frozen UV polymerization of the emulsion-templates stabilized by a low amount of surfactant, ACS Appl. Mater. Interfaces 10 (2018) 10147, https://doi.org/10.1039/C8RA01000E

[51] W. Zuo, X. Liu, J. Qiu, D. Zhang, Z. Xiao, J. Xie, F. Ren, J. Wang, Y. Li, G.F. Ortiz, W. Wen, S. Wu, M.-S. Wang, R. Fu, Y. Yang, Engineering Na+-layer spacings to stabilize Mn-based layered cathodes for sodium-ion batteries, Nat. Commun. 12 (2021) 4903, https://doi.org/10.1038/s41467-021-25074-9

[52] N. Bucher, S. Hartung, A. Nagasubramanian, Y.L. Cheah, H.E. Hoster, S. Madhavi, Layered Na_xMnO_{2+z} in sodium ion batteries–influence of morphology on cycle performance, ACS Appl. Mater. Interfaces 6 (2014) 8059–8065, https://doi.org/10.1021/am406009t

[53] X. Shu-Yin, W. Xiao-Yan, L. Yun-Ming, H. Yong-Sheng, C. Li-Quan, C. Novel, copper redox-based cathode materials for room-temperature sodium-ion batteries, Chin. Phys. B 23 (11) (2014) 118202, https://doi.org/10.1088/1674-1056/23/11/118202

[54] C. Wang, L. Liu, L. Zhang, Y. Peng, F. Zhou, Redox reactions of the α-synuclein–Cu^{2+} complex and their effects on neuronal cell viability, Biochemistry 49 (37) (2010) 8134–8142, https://doi.org/10.1021/bi1010909

[55] S. Altin, A. Bayri, E. Altin, E. Oz, S. Yasar, S. Altundag, M. Harfouche, S. Avci, Magnetic properties and environmental temperature effects on battery performance of $Na_{0.67}Mn_{0.5}Fe_{0.5}O_2$, Energy Technol. 9 (2021) 2001130, https://doi.org/10.1002/ente.202001130

[56] C. Chena, G.B. Liua, Y. Wang, J.L. Lia, H. Liu, Preparation and electrochemical properties of $LiFePO_4$/Cnanocomposite using $FePO_4{\cdot}2H_2O$ nanoparticles by introduction of $Fe_3(PO_4)_2{\cdot}8H_2O$ at low cost, Electrochim. Acta 113 (2013) 464–469, https://doi.org/10.1016/j.electacta.2013.09.095

[57] J.-Y. Li, X.-L. Wu, X.-H. Zhang, H.-Y. Lü, G. Wang, J.-Z. Guo, F. Wan, R.-S. Wang, Romanechite-structural $Na_{0.31}MnO_{1.9}$ nanofibers as high-performance cathode material for sodium ion battery, Chem. Commun. 51 (2015) 14848–14851, https://doi.org/10.1039/C5CC05739F

[58] M.N. Ates, Q. Jia, A. Shah, A. Busnaina, S. Mukerjee, K.M. Abraham, Mitigation of layered to spinel conversion of a Li-rich layered metal oxide cathode material for Li-ion batteries, J. Electrochem. Soc. 161 (2014) A290–A301, https://doi.org/10.1039/C5RA11665A

[59] L. Yang, Z. Liu, X. Shen, S. Li, Z. Hu, Q. Kong, J. Ma, J. Li, H.J. Lin, C.T. Chen, J.M. Chen, S.C. Haw, X. Wang, R. Yu, Z. Wang, L. Chen, Effect of vacancy-tailored Mn^{3+} spinning on enhancing structural stability, Energy Storage Mater. 44 (2022) 231–238, https://doi.org/10.1016/j.ensm.2021.10.024

[60] S. Altin, E. Oz, E. Altin, S. Demirel, A. Bayri, S. Avci, Investigations of the capacity fading mechanism of $Na_{0.44}MnO_2$ via ex situ XAS and magnetization measurements, Dalton Trans. 47 (2018) 17102–17108, https://doi.org/10.1039/C8DT03508C

[61] S. Altin, S. Altundag, E. Altin, E. Oz, M. Harfouche, A. Bayri, Investigation of Ti-substitution effects on structural and electrochemical properties of $Na_{0.67}Mn_{0.5}Fe_{0.5}O_2$ battery cells, Int. J. Energy Res. 44 (2020) 11794–11806, https://doi.org/10.1002/er.5820

[62] A. Bayri, E. Gocer, E. Altin, S. Altundag, E. Oz, M. Harfouche, S. Altin, S. Avci, $LiNi_{0.8}Co_{0.15}Ti_{0.05}O_2$: synthesis by solid state reaction and investigation of structural and electrochemical properties with enhanced battery performance, J. Mater. Sci: Mater. Electron 31 (22) (2020) 20527–20538, https://doi.org/10.1007/s10854-020-04572-4

[63] S. Altin, A. Bayri, S. Demirel, E. Oz, E. Altin, S. Avci, Structural, magnetic, electrical, and electrochemical properties of Sr–Co–Ru–O: a hybrid-capacitor application, J. Am. Ceram. Soc. 101 (2018) 4572–4581, https://doi.org/10.1111/jace.15698

[64] T. Gholam, L.R. Zheng, J.O. Wang, H.J. Qian, R. Wu, H.-Q. Wang, Synchrotron X-ray absorption spectroscopy study of local structure in Al-doped $BiFeO_3$ powders, Nanoscale Res. Lett. 14 (2019) 137, https://doi.org/10.1186/s11671-019-2965-3

[65] N.T. Taylor, F.H. Davies, I.E.M. Rudkin, C.J. Price, T.H. Chan, S.P. Hepplestone, ARTEMIS: Ab initio restructuring tool enabling the modelling of interface structures, Comput. Phys. Commun. 257 (2020) 107515, https://doi.org/10.1016/j.cpc.2020.107515

[66] H. Husain, M. Sulthonul, B. Hariyanto, C. Cholsuk, S. Pratapa, Technical aspects of EXAFS data analysis using Artemis software, Mater. Today.: Proc. 44 (2021) 3296–3300, https://doi.org/10.1016/j.matpr.2020.11.530

[67] H. Liu, X. Gao, J. Chen, J. Gao, S. Yin, S. Zhang, L. Yang, S. Fang, Y. Mei, X. Xiao, L. Chen, W. Deng, F. Li, G. Zou, H. Hou, X. Ji, Reversible OP4 phase in P2–$Na_{2/3}Ni_{1/3}Mn_{2/3}O_2$ sodium ion cathode, J. Power Sources 508 (2021) 230324, https://doi.org/10.1016/j.jpowsour.2021.230324